

E-PSS: the Extended Polarimetric Slope Sensing technique for measuring ocean surface waves

Nathan J. M. Laxague, *Member, IEEE*, Z. Göksu Duvarci,
Lindsay Hogan, Junzhe Liu, Christopher Bouillon, and Christopher J. Zappa

Abstract—Polarimetric slope sensing (PSS) is a powerful tool for remote measurement of the spatiotemporal characteristics of short surface waves. However, two key shortcomings have negatively impacted the widespread adoption of the technique: (1) the quality of the measurement may be sensitive to variability in environmental illumination conditions and (2) waves longer than the imager field of view are not reliably measured. We present an extension of PSS—namely, the Extended Polarimetric Slope Sensing (E-PSS) technique, which is robust to variation in ambient illumination conditions and provides simultaneous access to the directional spectrum for both long and short waves from a single surface-looking, narrow FOV camera.

Index Terms—Polarimetry, gravity-capillary waves, wave slope sensing, polarimetric slope sensing, division of focal plane

I. BACKGROUND

HERE is a long-standing and pressing need to measure the spatiotemporal characteristics of short-scale (wavelengths smaller than 10 m) surface waves. This is primarily driven by the intimate connection between these intermediate to small-scale waves and the local wind forcing: surface waves with wavelengths between 1 cm to 10 m support a significant fraction of the wave form drag, making them an essential mediator of air-sea momentum flux. It is fortuitous that radar-based remote sensing techniques operate with electromagnetic wavelengths in this very range; specifically, from HF radar down to k_u band microwave scatterometry. This enables indirect measurement of wave height, surface roughness, and wind forcing through interpretation of backscattered power.

However, the most commonly available techniques for measuring the surface wave field are unable to adequately characterize the energy or directionality of the surface wave field at scales shorter than 10 meters. Surface buoys are by far the most ubiquitous of *in situ* wave sensors, but even the small form-factor Spotter buoys do not provide reliable directional information beyond frequencies of 0.8 Hz (roughly corresponding to surface wave scales of 2 to 3 meters). This leaves a great deal of the surface wave spectrum which remains broadly inaccessible to observation. There are several techniques which have been developed to push the resolution of wave measurements to smaller and smaller scales. Perhaps

N. J. M. Laxague is with the Department of Mechanical Engineering and Center for Ocean Engineering, University of New Hampshire, Durham, NH, USA e-mail: Nathan.Laxague@unh.edu.

Z. G. Duvarci is with the Center for Ocean Engineering, University of New Hampshire; L. Hogan and C. J. Zappa are with Lamont-Doherty Earth Observatory of Columbia University; C. Bouillon is with Institut des Sciences de la Mer, Université du Québec à Rimouski, Rimouski, QC, Canada.

Manuscript received XXX; revised YYY.

the most widely adopted of these is stereophotogrammetry [1], [2]. This technique is able to recover the spatiotemporal characteristics of surface waves ranging in scale from 100 meters down to 50 centimeters. While this is quite impressive, it still does leave unresolved short-gravity and gravity capillary waves. Polarimetric slope sensing (PSS) was developed by Zappa and colleagues in 2008 [3] following decades of development of the application of classical optical theory towards inferring the shape of a free surface from the polarization state of light reflected off of it. PSS exploits the known (or at least, modeled) relationship between the polarization state of light reflected off an air-water interface and the geometry of the reflecting facet. When repeated spatially (over an imager field of view) and temporally (in short succession, as with video), one is able to recover the spatiotemporal evolution of the wave field down to very fine scales. Nevertheless—this technique is susceptible to variation in illumination conditions. And as initially presented, PSS could reliably measure the slopes of surface waves with wavelengths ranging from a few millimeters up to one meter (but in practice, rarely larger).

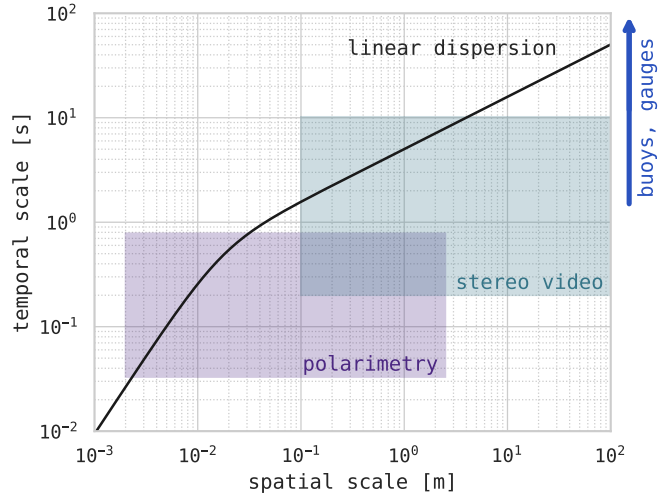


Fig. 1. Stommel diagram showing the spatiotemporal range of select wave measurement techniques: polarimetric slope sensing, stereo video, and point-like objects (buoys, fixed gauges). Note that the point-like objects provide no direct access to spatial information.

The Stommel diagram shown in Figure 1 compares the spatiotemporal ranges of select wave measurement techniques: PSS, stereo-video, and point-like gauges like buoys. In order to obtain a true spatiotemporal measurement of the surface wave field, it is important for the observational technique to envelop

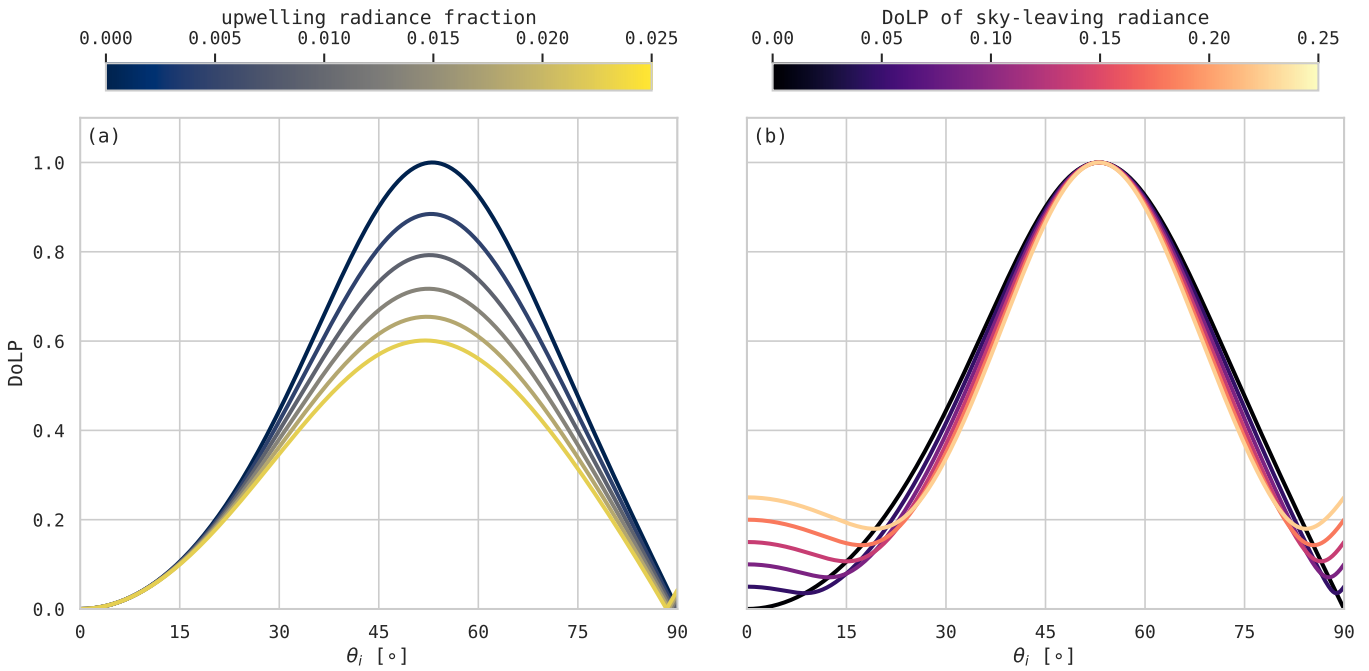


Fig. 2. Relationships between incidence angle (θ_i) and degree of linear polarization (DoLP) given variations in (a) fraction of received radiance which is upwelling and (b) DoLP of sky-leaving radiance.

the linear dispersion relation, here provided in the black curve on Figure 1. The violet shaded region corresponding to PSS is somewhat flexible: by increasing the imaging field of view (usually, through increasing the freeboard above the mean sea surface), one may shift the region to the right, therefore extending the effective maximally-resolvable temporal scale. Practitioners of wave-sensing stereophotogrammetry have extended the effective temporal window of the technique through time series analysis; e.g., Benetazzo *et al.* [2018] [4] employed the maximum entropy method (MEM) technique [5] to their surface elevation and slope estimates to infer the frequency-directional spectra of waves larger than the stereo field of view.

II. METHODOLOGY

The central assumption baked into the single-camera application of PSS is that sky-leaving radiance is unpolarized and upwelling (surface-leaving, but scattered from below the interface) radiance is negligible. This allows one to constrain the relationship between a measurement of degree of linear polarization (DoLP) and the incidence angle (θ_i) of the light ray. In practice, however, even small variations in ambient environmental conditions can have a significant impact on the relationship between the measured degree of linear polarization and the incidence angle that one might infer [6], [7]. In Figure 2(a), we show that even a small fraction of radiance which is upwelling and unpolarized can have a significant impact in compressing the DoLP that would be measured by an imaging polarimeter. Conversely, as shown in Figure 2(b), the effect of polarized sky-leaving radiance is to raise the floor of the variation of DoLP across all values of θ_i . The combined effect of variable sky-leaving and surface-leaving radiance is to modify this relationship. One approach to solving this problem might be to triple the number of imagers, including

in one's sensing suite a floating polarimeter for obtaining upwelling light measurements and a sky-oriented polarimeter for obtaining downwelling light measurements. This would allow one to incorporate these measured values into the Fresnel reflection coefficients and directly compute the relationship between DoLP and θ_i following Mueller calculus. However, one of the greatest benefits of polarimetric slope sensing is that it requires a single camera with no in-water component and no sky-looking camera. Adding additional requirements for in-water recovery of light polarization and sky-looking state would render the technique somewhat esoteric and limit it to specialists in the field of environmental optics. Another approach might be to have two cameras but rather than have one look at the sky and one at the surface we make a measurement of our slope field with a narrow field of view lens and have a second camera alongside it to make a direct measurement of the relationship between degree of linear polarization and incidence angle with a wide format lens. This direct measurement of $\text{DoLP}(\theta_i)$ would natively account for the sky leaving, the polarization state of sky leaving radiance and the fraction of light which comes up through the surfaced unpolarized. Furthermore, it would also implicitly account for path losses to the polarization state, making it an attractive option for airborne applications of polarimetric slope sensing. We will address the viability of that two-camera approach later in the manuscript. For now, we focus on attempting to solve our problem with a single downward-looking, narrow field of view camera, setting the task before us to correct for unpolarized upwelling radiance and polarized sky leaving radiance in a way that is robust, flexible, and does not depend on having multiple in water and sky looking imaging polarimeters.

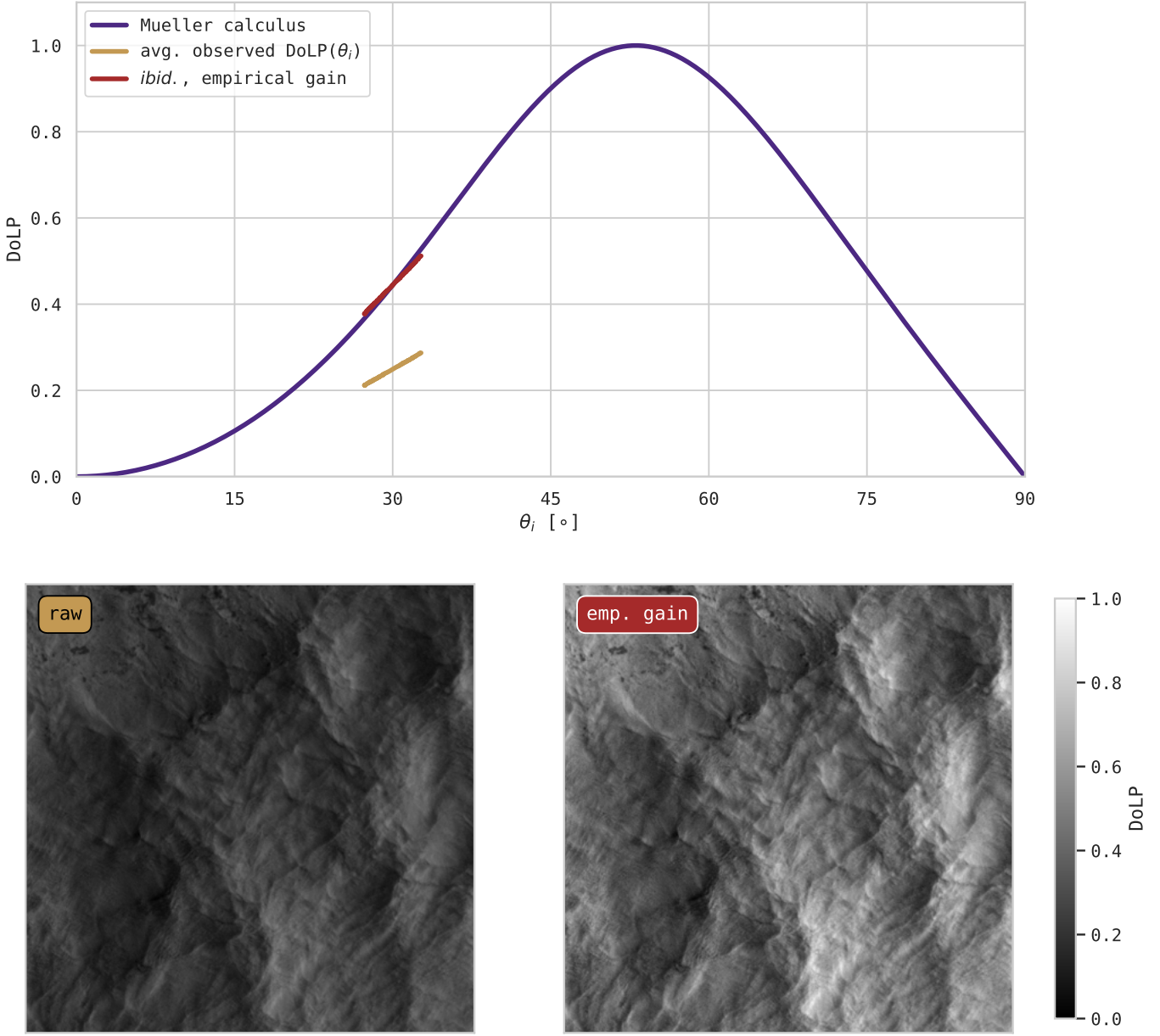


Fig. 3. Top: variation of degree of linear polarization (DoLP) with incidence angle (θ_i) as computed through Mueller calculus or observed via polarimetric camera. Bottom: spatial variation of DoLP provided no gain or an empirical gain.

Even under pristine laboratory conditions, a polarimeter may not perform ideally (that is, show ideal response when subjected to an integrating sphere/rotating linear polarizer test). This may be due to a number of factors, among them depolarization of light by optics or deviation of the sensor from optimal sensitivity. Correcting for these persistent effects is essential to making a good measurement [8], [9], [10], [11]. During integrating sphere polarizer tests of our DoFP detector, we found the normalized Stokes parameter amplitude to be 0.81 (rather than the ideal 1.0). The difference between S_1 and S_2 amplitudes was determined to not be statistically significant ($p = 0.74$, $N = 12$). We found the mean Stokes parameter to be slightly variable around zero (rms \approx 5%) with a directional asymmetry between minima and maxima of the Stokes parameters on the order of 2-3% of the amplitude.

This calibration is an important first step, though it will not

account for variability in the ambient illumination conditions. We demonstrate an empirical approach to accounting for variability in upwelling/downwelling radiance in Figure 3. The violet curve in the top panel represents the relationship between DoLP and θ_i which would arise due to unpolarized sky living radiance and no upwelling radiance (that is, the most simple form of Mueller calculus). The gold segment on that panel corresponds to the observed variation of DoLP from the bottom to the top of the image frame as averaged over a single ten-minute period. The range of θ_i is obtained directly from the known mounting geometry of the instrument and the vertical angle of view for the camera-lens combination (here $30^\circ\pm2.7^\circ$ for a 75 mm lens).

A corresponding snapshot of the full-frame DoLP is given in the bottom left panel, marked with a label of “raw”. The *empirical gain* is simply the value by which the frame-

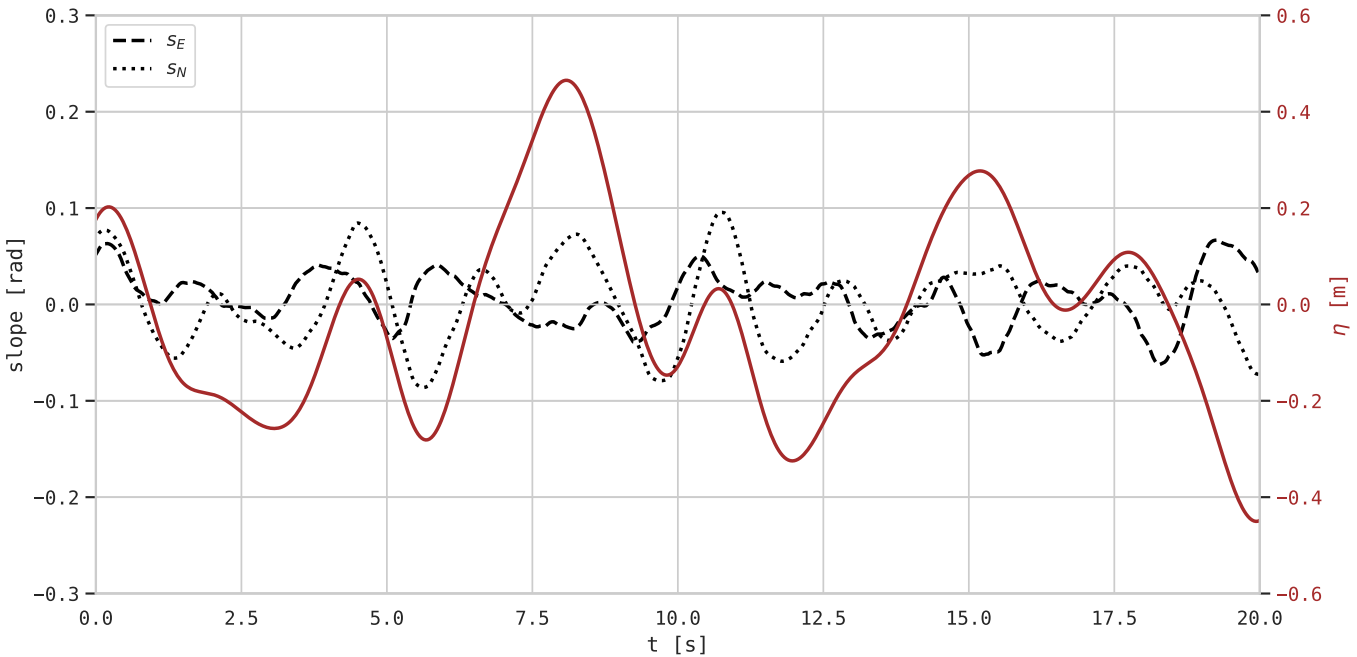


Fig. 4. Temporal variation of east and north wave slope (s_E & s_N , respectively) along with the corresponding water surface elevation η computed via the Fourier space inversion approach of equation 1.

median DoLP needs to be scaled in order to yield the value expected for zero upwelling radiance and unpolarized sky-leaving radiance. After application of the empirical gain to the time-averaged DoLP, we obtain the red segment in the top panel. When that gain value is applied to the DoLP snapshot, we obtain the field shown in the bottom right panel.

Absent supporting independent information regarding upwelling and sky-leaving radiance, this empirical approach seems to be the most straightforward: the known orientation of the camera defines the slope reference on a case-by-case basis. Nevertheless, it is important that we demonstrate the positive impact of this approach. The best way to accomplish this would be to have a secondary measurement that could act as a gold standard; however, the principal benefit of PSS is that it is the sole established technique for field observations of short to intermediate-scale ocean waves. During the Fall and Winter of 2019-2020, a set of targeted measurements of wind forcing, surface waves, and near-surface currents were made at the Air-Sea Interaction Tower (ASIT) just south of Martha's Vineyard, MA [11]. As part of this campaign (hereinafter "ASIT2019"), we obtained wind speed and turbulent fluxes along with the water surface elevation time series via near-infrared LiDAR. For some observational cases, we also obtained the frequency-directional wave spectrum via bottom-mounted ADCP. In order to demonstrate the efficacy of the empirical gain approach, we will compare the wave height and mean wave period obtained via LiDAR measurements to the same quantities inferred from surface slope field measurements.

The first step in this comparison is to infer the water surface elevation time series from the time series of two-component surface slope, as in equation 1:

$$\eta(t) = \mathcal{F}^{-1} \left\{ -\frac{i}{k} [\mathcal{F}\{s_E\} + \mathcal{F}\{s_N\}] \right\} \quad (1)$$

This inversion follows directly from small-amplitude (linear) water wave theory. It is analogous to orbital velocity/pressure inversion techniques [12], and can be thought of as a one-dimensional application of the slope field inversion technique of Frankot & Chellappa [13]. A demonstration of this approach is presented in Figure 4. The east and north oriented slope components are provided as dashed and dotted curves, respectively, while the red trace indicates the resulting water surface elevation time series η inferred from the slope time series. The corresponding omnidirectional frequency spectra are provided in Figure 5. Note that the frame size of $L \approx 3$ m limits the proper frequency response above 0.35 Hz (wavelength $\approx 4L$).

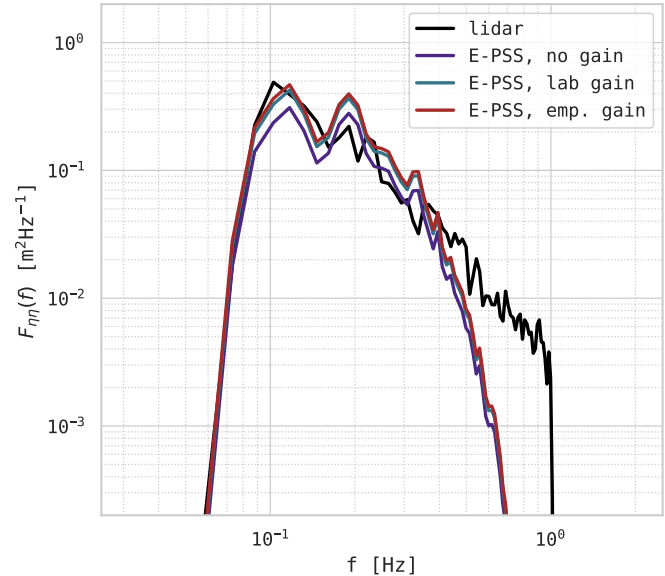


Fig. 5. Omnidirectional spectra computed from water surface elevation timeseries obtained by LiDAR and E-PSS.

201

III. RESULTS

202 From this point forward, we use the acronym E-PSS (Ex-
 203 tended Polarimetric Slope Sensing) to describe a combina-
 204 tion of (1) polarimetric slope sensing with a laboratory or
 205 empirically-based modification to the $\text{DoLP}(\theta_i)$ relationship
 206 and (2) the estimation of surface elevation via Fourier space
 207 inversion of the slope time series. As shown in Figure 2b,
 208 unpolarized sky-leaving radiance will elevate the lowest degree
 209 of linear polarization that will be observed from a downward-
 210 looking imaging polarimeter. However, we did not find there
 211 be an elevated floor the measurements of DoLP made over a
 212 range of ambient conditions (full sun to full overcast) during
 213 the 2019–2020 ASIT field campaign. To be specific, we found
 214 frequent occurrence of low (<0.1) values of DoLP for all
 215 ambient illumination conditions, indicating that variability in
 216 sky-leaving polarization state is likely to be of secondary
 217 importance for PSS. However, given the somewhat large
 218 values of empirical DoLP gain (1.2–1.7) used during our field
 219 observations, upwelling radiance should not be neglected. This
 220 is consistent with previous studies of upwelling radiance [14],
 221 [15]. Based on the values provided in Figure 2a, it's reasonable
 222 to expect that between 1–3% of the radiance received by our
 223 imaging polarimeter is unpolarized, upwelling radiance that
 224 is diluting the measurement that we would be making from
 225 surface reflected light. This would indicate that an approach
 226 which allows for a variable gain (e.g., our empirical approach)
 227 to have a significant advantage over the static laboratory-based
 228 calibration.

229 The benefit of using an empirical gain approach is demon-
 230 strated in the scatter plot of Figure 6, wherein we compare
 231 the significant wave height computed from LiDAR and E-PSS-
 232 derived wave spectra. We compute the significant wave height
 233 as four times the square root of the zeroth moment of the wave
 234 spectrum, $H_{m0} = 4 \times \left(\int_0^\infty F(f) df \right)^{1/2}$.

235 The figure legend contains pieces of key statistical infor-
 236 mation about the comparison between LiDAR and E-PSS
 237 estimates. The no-gain and laboratory-gain approaches provide
 238 significant wave heights which are substantially lower than
 239 those produced from the LiDAR measurements. However,
 240 the H_{m0} estimates produced via empirical gain approach are
 241 appropriately close to those obtained by LiDAR: $R^2 \approx 0.76$,
 242 RMSE ≈ 32 cm, and a fit slope of 0.98, indicating nearly
 243 one-to-one response. An analogous comparison is provided in
 244 Figure 7, where we show the mean wave period computed
 245 both from LIDAR and E-PSS measurements. The mean wave
 246 period (T_{m02}) is defined in the following manner:

$$T_{m02} \equiv \left(\frac{m0}{m2} \right)^{1/2} = \left(\frac{\int_0^\infty F(f) df}{\int_0^\infty f^2 F(f) df} \right)^{1/2} \quad (2)$$

247 Note that the E-PSS estimate of T_{m02} is less sensitive
 248 than H_{m0} to the DoLP gain value: the frequency response
 249 is weakly sensitive to the choice of gain, whereas the total
 250 energy contained within the spectrum is quite sensitive to the
 251 gain. The underestimation of T_{m02} by E-PSS for moderate to
 252 long wave periods is likely due to the method's performance at
 253 low frequencies. The Fourier space transfer function between

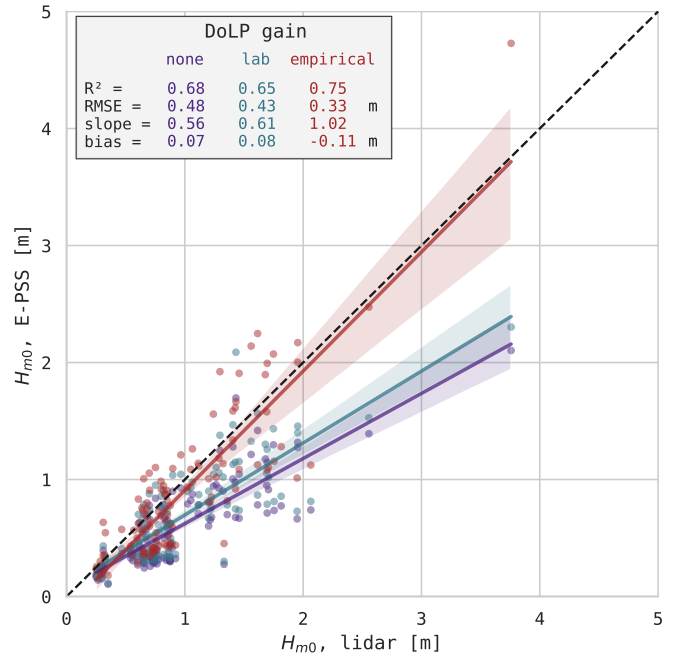


Fig. 6. Scatterplot comparing significant wave height (H_{m0}) estimates from lidar and E-PSS for each of the three DoLP gain values. Dots mark individual observations while lines represent the least-squares linear fits (with shaded regions demarcating 95% confidence intervals). Key error metrics (computed with respect to H_{m0} , lidar) are given in the figure legend.

242 slope and surface elevation goes like $k^{-1} \propto f^{-2}$, requiring a
 243 somewhat aggressive highpass filter to curtail spuriously-high
 244 energy at low frequencies. We established a passband of 0.08
 245 Hz $\leq f \leq 1$ Hz; however, application of a lowpass filter is
 246 somewhat redundant due to the spatial averaging inherent to
 247 the process of computing the mean slope over our 2.5 m \times
 248 2.5 m field of view ($f_{cut} \approx 0.75$ Hz).

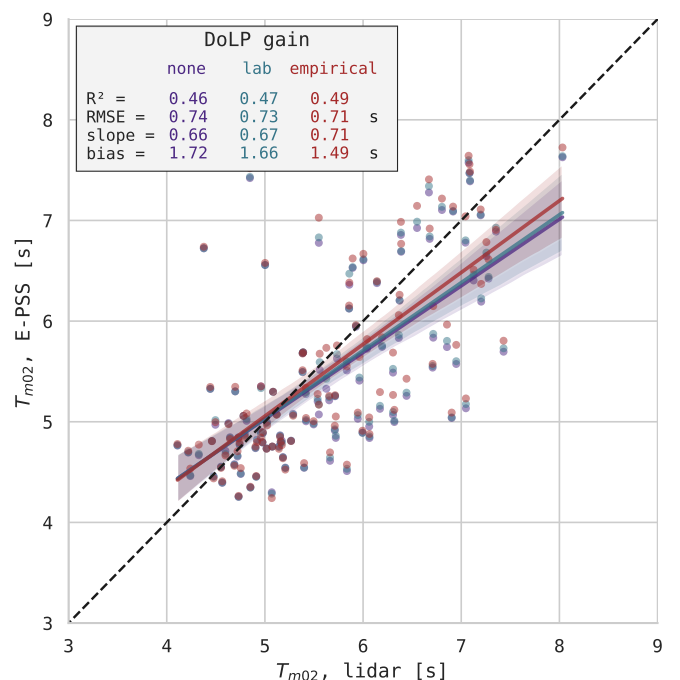


Fig. 7. Analogue to Figure 7 for mean wave period (T_{m02}).

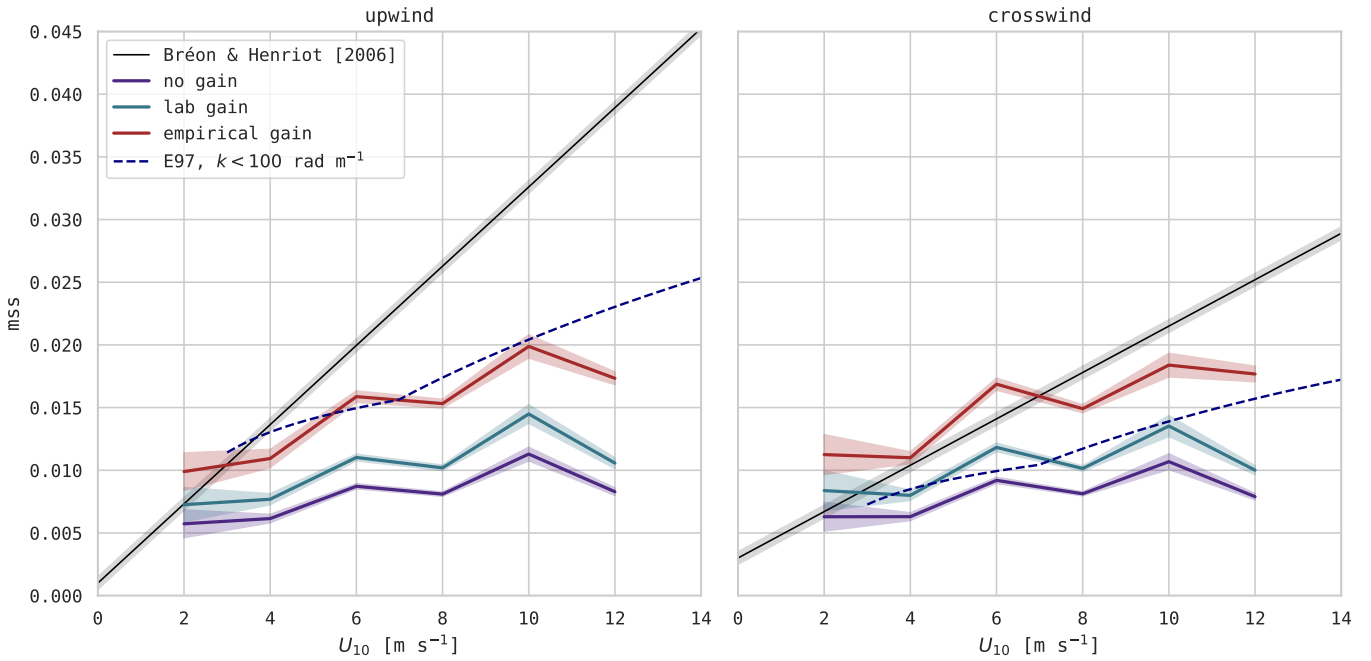


Fig. 8. Upwind and crosswind mean square slope computed from wave slope fields given the three modes of DoLP gain application. Shaded regions demarcate the 95% confidence interval about the mean. Black lines and shaded regions represent the least-squares fits and uncertainties of Bréon & Henriot [2006]. The dashed blue trace marks values of *mss* computed from the spectrum of Elfouhaily *et al.* [1997] [16] assuming a high wavenumber cutoff of 100 rad m⁻¹.

The joint probability density function (PDF) for upwind and crosswind wave slope is approximately Gaussian. In the real ocean, wind stress and long surface waves impact the short wave slope distribution in a way that yields non-zero skewness and kurtosis (peakedness). Cox & Munk [1954] accounted for this by providing a Gram-Charlier polynomial expansion about a Gaussian distribution [17], here provided in equation 3:

$$P(\xi, \zeta) = \frac{1}{2\pi\sigma_{up}\sigma_{cr}} \exp\left(-\frac{\xi^2 + \zeta^2}{2}\right)$$

$$\cdot \left\{ 1 - \frac{1}{2}c_{21}(\xi^2 - 1)\zeta \right. \\ \left. - \frac{1}{6}c_{03}(\zeta^3 - 3\zeta) \right. \\ \left. + \frac{1}{24}c_{40}(\xi^4 - 6\xi^2 + 3) \right. \\ \left. + \frac{1}{24}c_{04}(\zeta^4 - 6\zeta^2 + 3) \right. \\ \left. + \frac{1}{4}c_{22}(\xi^2 - 1)(\zeta^2 - 1) \right. \\ \vdots \quad \right\} \quad (3)$$

We omit the expansion's higher-order terms. The quantities σ_{up} and σ_{cr} correspond to the standard deviations about the mean of upwind and crosswind slopes, respectively. The independent variables of the distribution, ξ and ζ , represent the crosswind and upwind wave slopes normalized by the corresponding wave slope standard deviation.

The variation of upwind and crosswind mean square slope (i.e., σ_{up}^2 and σ_{cr}^2 , respectively) with ten-meter wind speed U_{10} observed during ASIT2019 is provided in Figure 8. The three different colored segments indicate measurements of mean square slope obtained from E-PSS given the three

aforementioned DoLP gain modes (no gain, laboratory-derived gain, empirical gain). Shaded regions on the three colored curves from our measurements correspond to 95% confidence intervals about the mean. The black line marks the results of Bréon & Henriot [2006] [18] which are in close agreement with the classic Cox & Munk [1954] [17] observations. The shaded region about the black lines correspond to Bréon & Henriot's reported level of uncertainty. The blue dashed trace represents upwind/crosswind slope variance computed from the wavenumber-directional spectrum of Elfouhaily *et al.* [1997] [16] assuming a high wavenumber cutoff of 100 rad m⁻¹.

The joint PDF for upwind and crosswind wave slope was computed for all ASIT2019 observational cases with the three aforementioned DoLP gain modes. From these we obtained the marginal PDFs: the upwind slope PDF and the crosswind slope PDF. A selection of these (bin-averaged by ten-meter wind speed U_{10}) are shown alongside the Bréon & Henriot [2006] [18] marginal PDFs in Figure 9. We performed a least-squares fit to each wave slope joint PDF, specifying the functional form as the Gram-Charlier expansion of a Gaussian (equation 3). This exercise yielded the coefficients c_{21} & c_{03} (corresponding to skewness) and c_{40} , c_{04} , & c_{22} (corresponding to kurtosis). We present these coefficients in Figure 10, bin-averaged by ten-meter wind speed U_{10} and shown alongside the results of Bréon & Henriot [2006] [18] and Cox & Munk [1954] [17]. Colored segments correspond to the results of E-PSS, with shaded regions representing the 95% confidence interval about the mean. The shaded regions around the black traces of Bréon & Henriot correspond to their empirically derived levels of uncertainty. In panel (f) we provide the number of samples per wind speed bin ranging from 10 to 40 per wind speed bin.

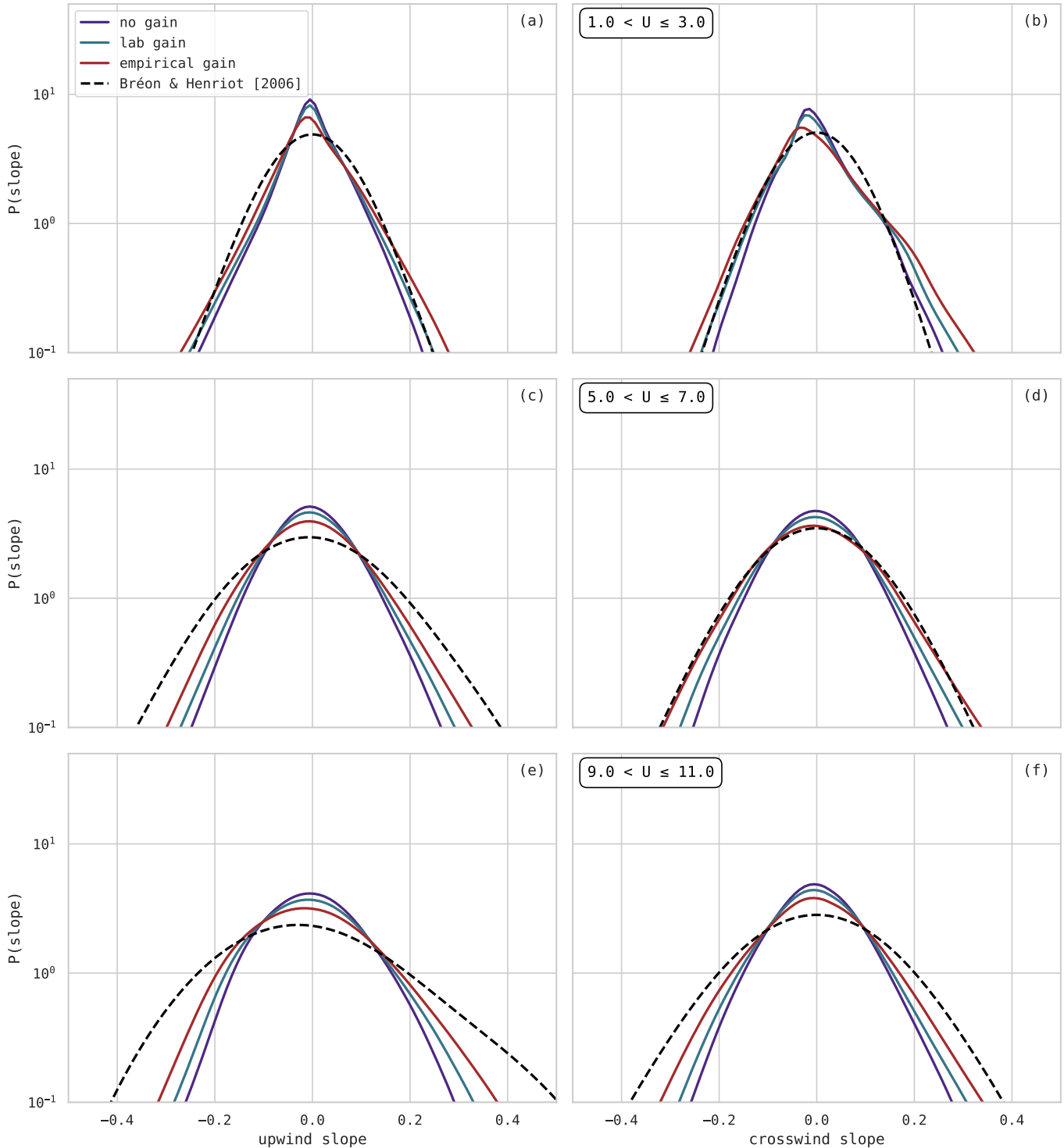


Fig. 9. Slope probability density functions, upwind (a,c,e) and crosswind (b,d,f). Colored traces correspond to PDFs produced from field observations with varying DoLP gain values. Black dashed traces correspond to Gram-Charlier distribution with coefficients taken from Bréon & Henriot [2006].

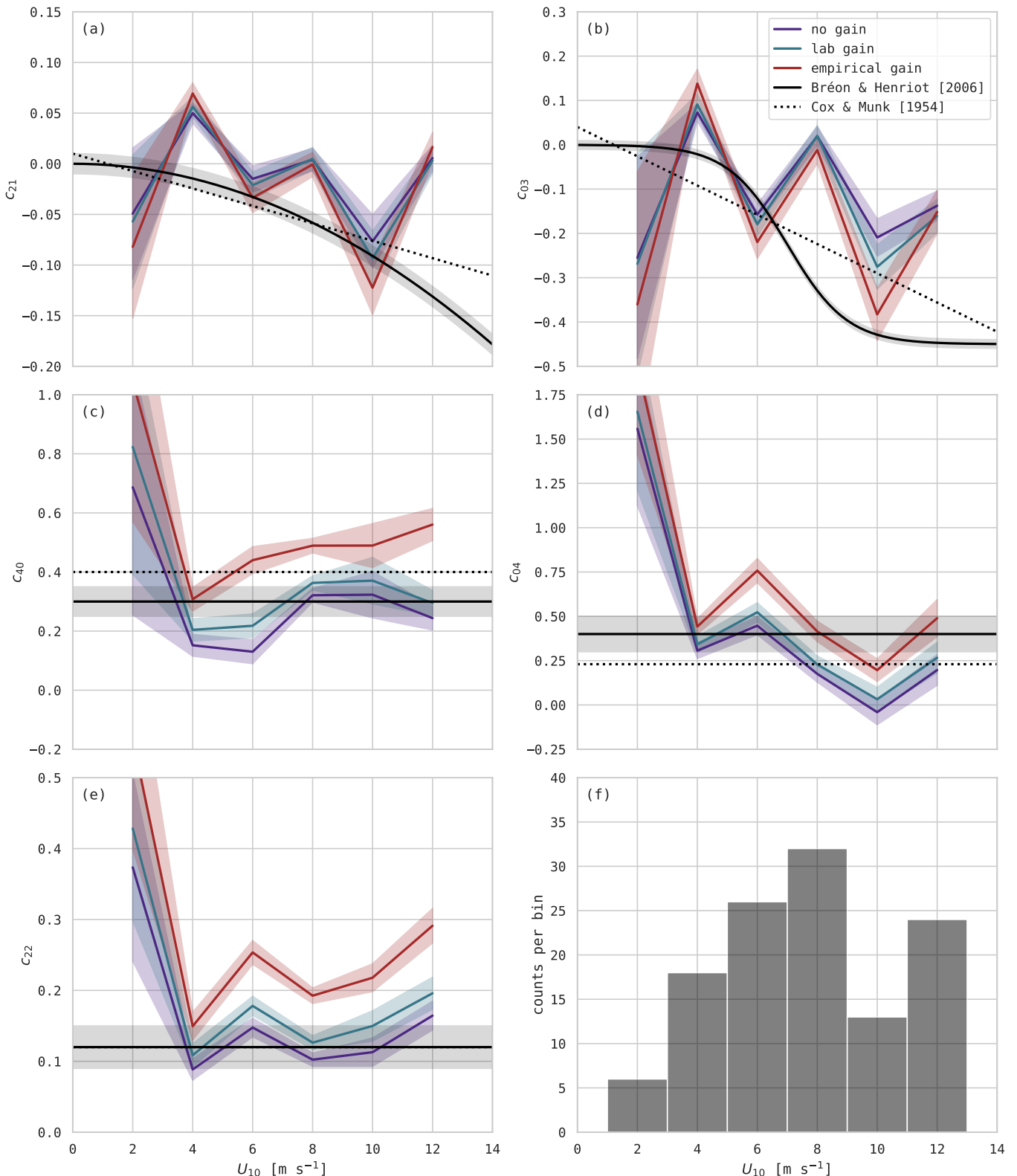


Fig. 10. Coefficients c_{ij} of the Gram-Charlier expansion to the 2D Gaussian wave slope distribution. Coefficients correspond to skewness (c_{21} & c_{03}) and kurtosis (c_{40} , c_{04} , & c_{22}) of the distribution. Colored traces represent values averaged in bins equally-spaced in wind speed, with shaded regions marking the 95% confidence interval about the mean. Black curves represent least-squares fits from Bréon & Henriot [2006], with shaded region marking the qualitatively-determined uncertainty [18]. Bar chart in panel (f) displays sample size per wind speed bin.

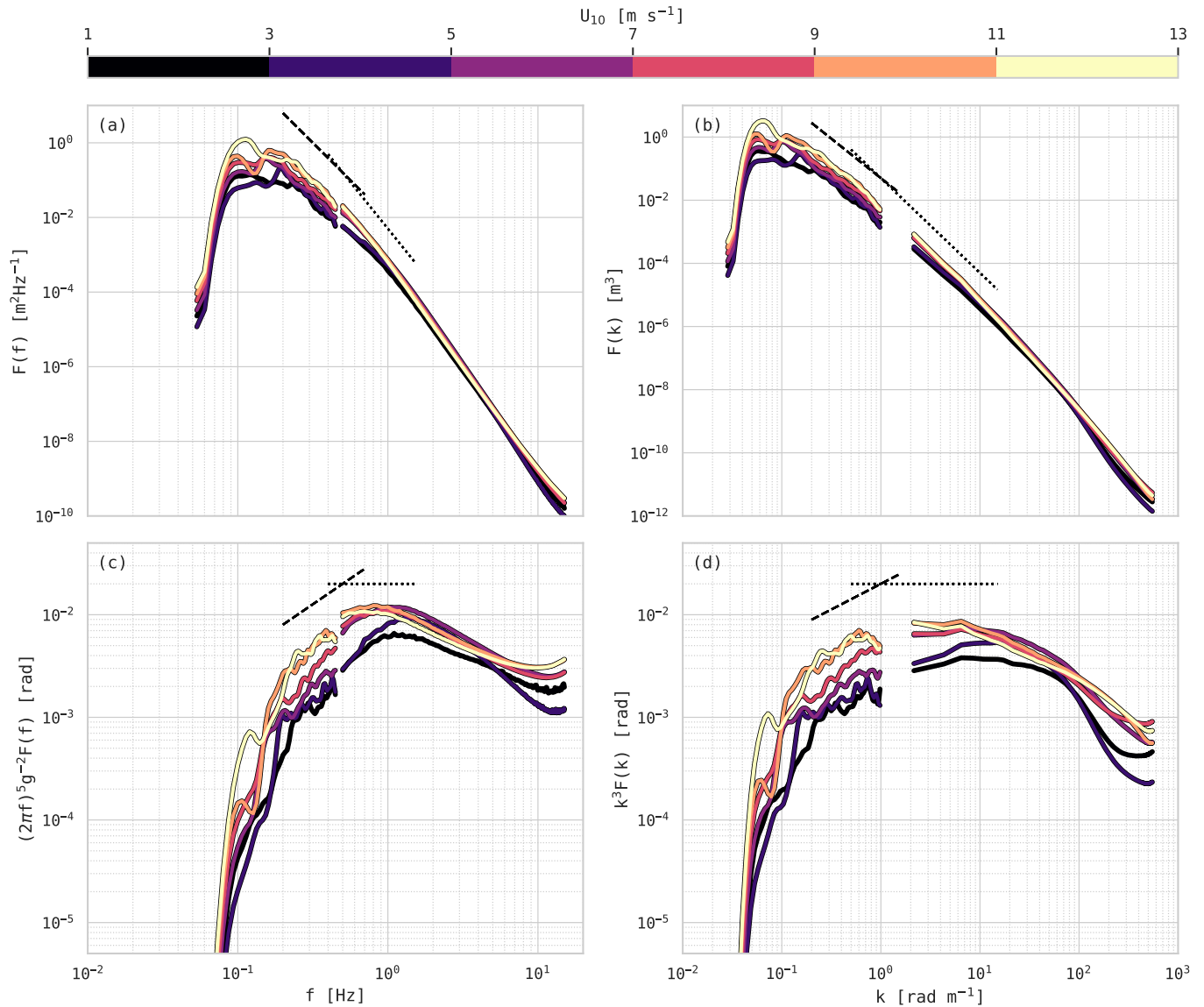


Fig. 11. Omnidirectional spectra: (a) frequency elevation, (b) wavenumber elevation, (c) frequency saturation, (d) wavenumber saturation. Color indicates the ten-meter wind speed range for which each bin average was computed. Dashed and dotted lines correspond to power laws indicating the slope to be expected in the equilibrium (f^{-4} , $k^{-2.5}$ elevation; f^1 , $k^{0.5}$ saturation) and saturation (f^{-5} , k^{-3} for elevation; f^0 , k^0 saturation) ranges, respectively.

As demonstrated in section II (and shown in Figure 5), E-PSS allows one to infer the elevation omnidirectional frequency spectrum from the wave slope time series. We found good response for frequencies f on [0.08 Hz, 0.5 Hz]. For the slope field size L^2 of $2.91 \text{ m} \times 2.91 \text{ m}$ obtained during ASIT2019, this range of frequencies corresponds to waves with wavelength λ on $[2L, 50L]$. Polarimetric slope sensing is capable of obtaining the “direct” wavenumber-frequency directional spectrum for waves in the range of scales constrained by the sampling rate, camera resolution, and spatial frame size. For this field campaign, the sampling rate of 30 fps and effective spatial resolution of 5.69 mm/px limited the Nyquist frequency and wavenumber to 15 Hz and $551.74 \text{ rad m}^{-1}$, respectively.

The omnidirectional wave spectra obtained via E-PSS during ASIT2019 are shown in Figure 11. The “direct” frequency spectra were subjected to band-averaging while the spectra produced from the inferred sea surface elevation were computed using Welch’s method (one-minute non-overlapping segments, each subjected to a Hann window). Spectra have been averaged in wind speed bins of 2 m s^{-1} in U_{10} (as indicated by the color bar). The top row contains elevation spectra while the bottom row contains saturation spectra (i.e., compensated by f^5 or k^3). Dashed and dotted lines correspond to the equilibrium and saturation ranges, respectively. The wavenumber spectra for long waves was inferred through linear wave theory, given the water depth at ASIT of 15 meters and assuming no current.

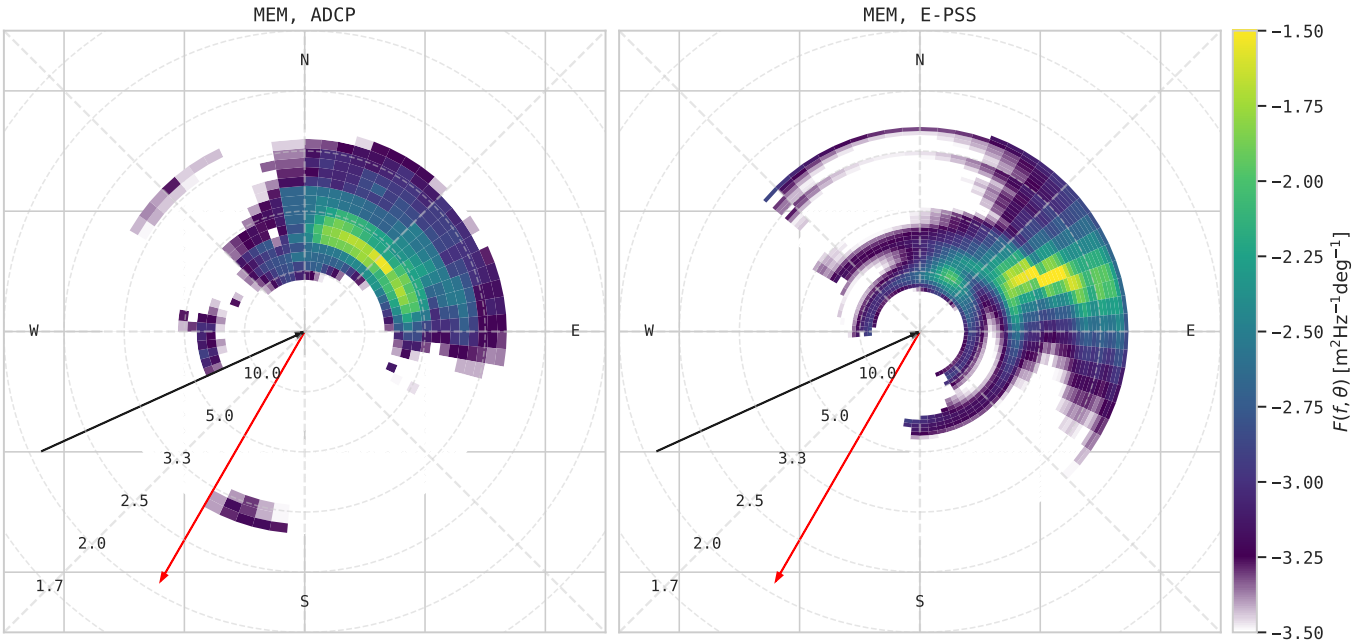


Fig. 12. Frequency-directional spectra computed via MEM given (a) the surface elevation/current profile measurements of the ADCP and (b) the measured two-component long wave slope and water surface elevation inferred via E-PSS. The black arrow indicates the wind direction ($U_{10} = 7.7 \text{ m s}^{-1}$) and the red arrow indicates the surface current direction ($U_{sfc} = 0.11 \text{ m s}^{-1}$, $z_{sf} \approx 1 \text{ cm}$). Wave and current direction is provided in “going-to” convention, while wind direction follows the meteorological “coming-from” convention.

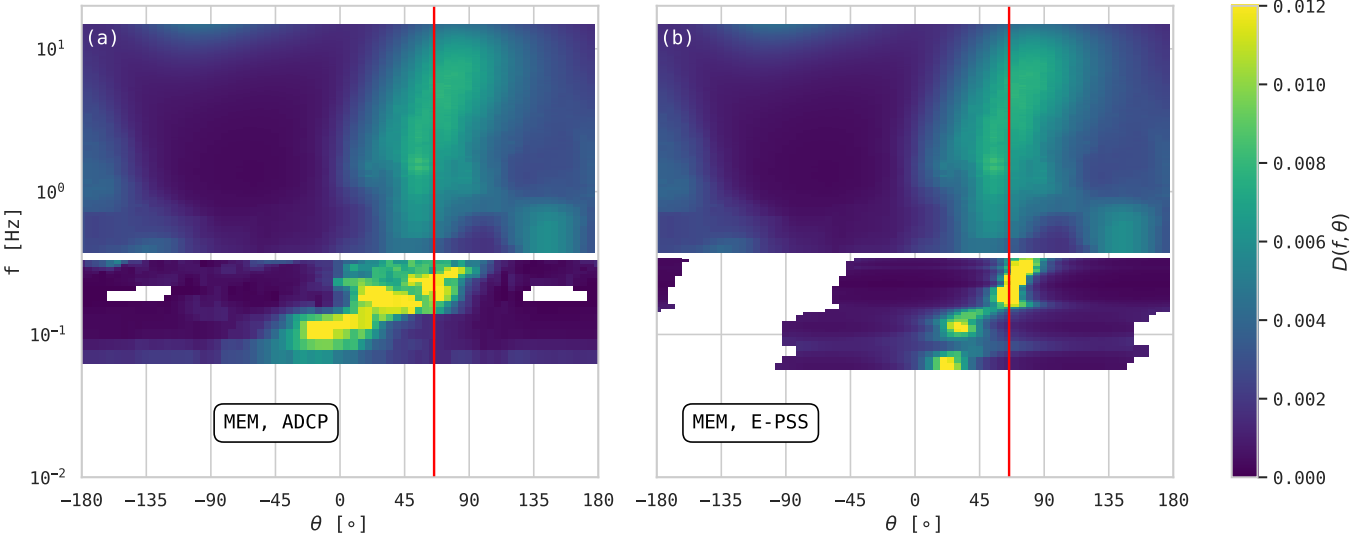


Fig. 13. Frequency-directional wave distribution $D(f, \theta)$ corresponding to the case shown in Figure 12: (a) ADCP via MEM, (b) E-PSS via MEM, and (top half of a,b) directly from the wave slope field 3D Fourier transform. The red line indicates the wind direction in “going-to” convention.

322 A pair of example frequency-directional wave spectra is
 323 shown in Figure 12. The left panel contains the directional
 324 wave spectrum obtained from our Teledyne RDI Sentinel V
 325 ADCP [19], while the right panel contains the directional
 326 wave spectrum inferred from the surface elevation and slope
 327 measurements of E-PSS. Each spectrum was produced using
 328 the maximum entropy method (MEM) [5]. Color corresponds
 329 to the base 10 logarithm of the spectral energy density. The
 330 black arrow gives the direction of the wind, while the red
 331 arrow provides the direction of the near surface current.
 332

Given the frequency-directional spectrum $F(f, \theta)$,

the wave directional distribution $D(f, \theta)$ is defined as:

$$D(f, \theta) \equiv \frac{F(f, \theta)}{F(f)} \quad (4)$$

... where $F(f) = \int_{-\pi}^{\pi} F(f, \theta) d\theta$ is the omnidirectional frequency spectrum. Figure 13 contains $D(f, \theta)$ computed from the frequency-directional spectra shown in Figure 12. The top portion of panels (a-b) correspond to the frequency directional spectra obtained directly from the water surface slope field “stacks”. The bottom portion of those panels correspond to the directional spectra obtained via MEM from either the ADCP or E-PSS measurement.

333
334
335
336
337
338
339
340

Following Lin *et al.* [2021] [20], we calculate mean wave direction θ_0

$$\theta_0(f) = \int_{-\pi}^{\pi} \theta D(f, \theta) d\theta \quad (5)$$

... and spreading width σ_θ

$$\sigma_\theta(f) = \left[\int_{-\pi}^{\pi} (\theta - \theta_0)^2 D(f, \theta) d\theta \right]^{1/2} \quad (6)$$

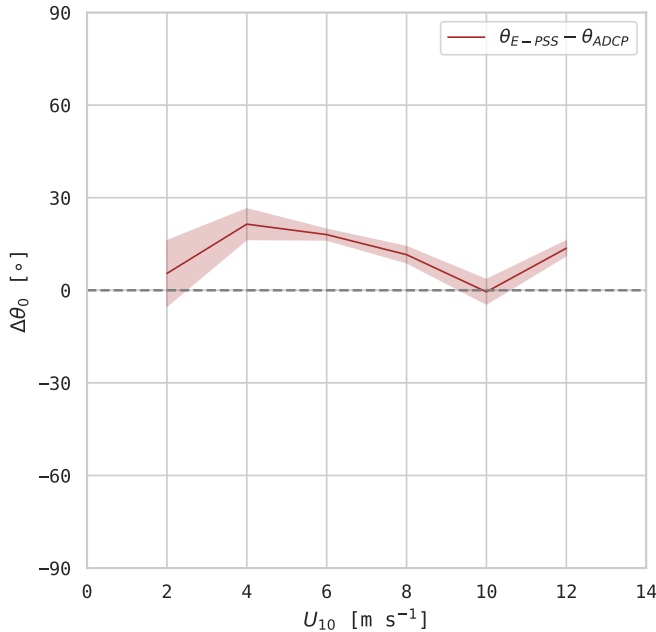


Fig. 14. Difference in mean wave direction θ_0 computed from ADCP and E-PSS directional spectra.

The mean wave direction and directional spread may alternatively be computed from the first-order Fourier moments [21]. However, we computed $\theta_0(f)$ and $\sigma_\theta(f)$ from the spectra themselves in order to maintain consistency of approach between the ADCP and E-PSS datasets. This approach carries the additional benefit that it would also be usable with the “direct” frequency-directional spectra obtained from the wave slope fields themselves.

In Figure 14, we show the difference in mean wave direction $\Delta\theta_0$, with each θ_0 computed from the ADCP and E-PSS directional spectra via equation 5. Values of $\Delta\theta$ were bin-averaged by ten-meter wind speed U_{10} , with bin centers/spacing following the convention used here up to this point. The red shaded region marks the 95% confidence interval about the mean. Equation 6 provides the means to compute the wave directional spreading width $\sigma_\theta(f)$. A direct intercomparison of mean wave direction estimates does strain our capability: there is a substantial spatial separation (≈ 1 km laterally) between the ADCP mooring and ASIT. More to the point, the ADCP mooring was on the 18.3-meter isobath while ASIT is on the 15-meter isobath. We attempted to correct for the latter effect (assuming simple refraction) via Snell’s law, though this correction appears to have been negligible. In Figure 15(a), we show an example $\sigma_\theta(f)$ computed from the spreading functions $D(f, \theta)$ obtained by ADCP and E-PSS for a particular run. The red vertical segment corresponds to the frequency the energy-weighted mean frequency, $f_E = m_{-1}/m_0$. In panel (b), we provide the bin averaged response of $\sigma_\theta(f_E)$ as a function of 10 meter wind speed U_{10} . Shaded regions correspond to the 95% confidence intervals about the mean.

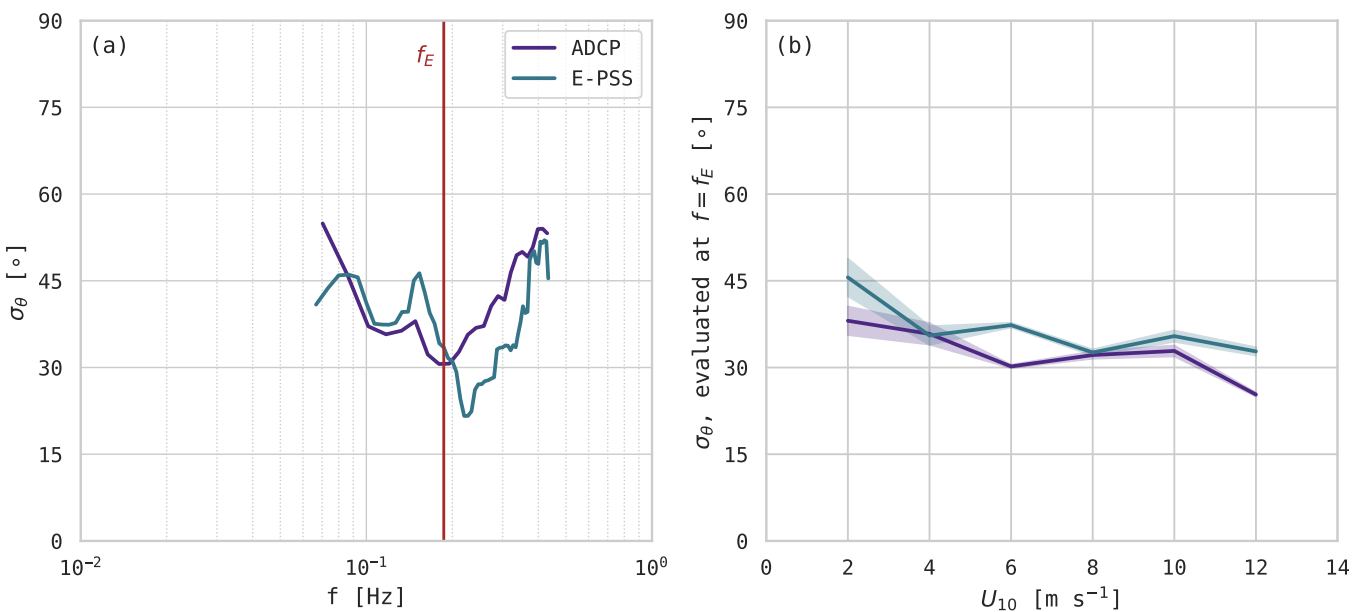


Fig. 15. Spreading width σ_θ , computed from $D(f, \theta)$ obtained from ADCP and E-PSS spectra following eq. 6 for (a) a single case (the one shown in Figures 12-13) and given in terms of frequency and (b) all cases, bin-averaged and evaluated at the energy-weighted mean frequency f_E ; shaded regions demarcate 95% confidence intervals about the mean.

371

IV. DISCUSSION

372

A. Core findings of this paper

373

The results shown in Figure 6 (H_{m0}) and Figure 8 (mss) demonstrate that it is essential to characterize the polarization response of one's polarimetric camera— and that failure to properly account for ambient environmental conditions may have a substantial negative impact on the measured slope magnitude. Our simple, single-camera “empirical” correction to the observed DoLP allows E-PSS to provide a reasonable estimate of the significant wave height H_{m0} . A recent intercomparison [22] between directional wave spectral estimates provided by different types of wave buoy systems (e.g., NOAA 3DMG, HIPPY, Triaxys, Watchman, and Datawell DWR) showed that for H_{m0} , it is reasonable to expect biases of approximately 0.1 m and RMSE of approximately 0.3 m. These values are almost exactly the error metrics we find for E-PSS relative to our reference lidar system, despite the enormous disparity in sample size between the two studies (order 10^4 for the buoy study, order 10^2 here). The buoy intercomparison estimates of mean wave period T_{m02} are far more closely clustered than our E-PSS and lidar values, though we attribute the underestimation of mean wave period to the slight underestimation of wave energy at very low frequencies (as described in section III).

395

The empirical gain approach appears to improve the estimate of mean square slope (Figure 8), though our observed values are still lower than classic observations [17], [18] for moderate wind speeds ($U_{10} \geq 7 \text{ m s}^{-1}$). It may be the case that these relatively low values of mss are owed to a degraded effective resolution of our polarimeter: for division of focal plane (DoFP) polarimeters like the one used in this study, one should expect a steep falloff in spectral energy density for scales 5-10 times larger than the image resolution [11]. We have computed the upwind and crosswind slope variance from the model wavenumber-directional spectrum of Elfouhaily *et al.* [1997] [16], setting the wavenumber upper limit of integration to 100 rad m $^{-1}$. It appears that this effective resolution limitation [11] is a reasonable explanation for the relatively low wave slope variance observed here. The marginal wave slope PDFs (Figure 9) reveal that slopes with absolute value greater than 0.3 are extraordinarily rare at moderate wind forcing, even with the empirical DoLP gain. Waves of such extreme slopes tend to be exceptionally short— e.g., sub-centimeter, in the short gravity-capillary and pure capillary regime. This low level of detection of ultra-steep waves is further evidence that the shortest waves are systematically underresolved [11]. In contrast, the sun glint-based statistical results of Cox & Munk and Bréon & Henriot capture the total effect of surface waves to contribute to reflectance— though those results do not provide insight into the scale dependence of the reflectance. It is this scale awareness of E-PSS—both in space and time—that makes the technique so valuable.

423

Higher-order statistics (skewness and kurtosis) were estimated from the coefficients inferred through a least-squares fit of a Gram-Charlier expansion to the 2D Gaussian wave slope distribution; these are provided in Figure 10. The effect of the DoLP gain on the computed wave slope skewness and

kurtosis is inconclusive; it may be that the modest binned sample size of the present dataset (Figure 10) is insufficient to the task of parsing the behavior of these higher-order statistics given fine-grain adjustments to the measured light polarization state. Indeed, there is significant uncertainty in those parameters even as obtained from the large sample size satellite dataset used by Bréon & Henriot [2006]. Nevertheless, the skewness and kurtosis values produced from the ASIT2019 field campaign are generally comparable to the classically-accepted values.

The combined omnidirectional spectra provided in Figure 11 demonstrate the dual capabilities of E-PSS in providing a reliable measurement of both short waves and long waves. The polarization measurements used to compute the slope fields from which the spectra were produced were subjected to the empirically-derived DoLP gain. However, no further adjustments to the spectra were performed. The strong agreement in both spectral energy density and spectral subrange slope between the “direct” omnidirectional spectra and those inferred from the long wave time series is a natural consequence of the internal consistency of E-PSS.

We sought to examine the ability of E-PSS to recover long wave directionality by computing the frequency-directional spectrum via MEM [5] given the two-component wave slope and water surface elevation. Use of an established technique like MEM confines our focus to the task of evaluating E-PSS itself. However, we note that the outputs of two-component wave slope and water surface elevation affords the technique a great deal of flexibility with respect to ultimate application. In particular, it opens E-PSS to a wide range of tools for evaluating wave directionality, including novel open-source utilities with the ability to capture nonstationarity in the wave field [23], [24]

The wave frequency directional spectra shown in Figures 12 & 13 provide a snapshot into the performance of E-PSS for capturing long wave directionality. Although it is difficult to say for certain without a third reference measurement, the smearing which occurs at the peak frequency in the ADCP-derived directional spectrum is likely a limitation of that particular measurement, whereas the directional veering we see in the E-PSS-derived spectra appears to track from the dominant long wave direction into the wind direction for shorter scales. As shown in Figure 13, this alignment of intermediate-to-short gravity wave scales into the wind direction is consistent between the long wave and short wave (“direct”) portions of the E-PSS spectra. It is reasonable to expect some difference in mean wave direction between the ADCP-derived and E-PSS-derived spectra. In Figure 14, we see that this deviation is largest for low to moderate levels of wind forcing, but quite small (reliably less than 10° for higher levels of wind forcing ($U_{10} \geq 8 \text{ m s}^{-1}$)). We note that the aforementioned buoy intercomparison [22] found a mean difference in Fourier coefficient-derived $\bar{\theta}$ (analogous to our θ_0) between buoys in the same location of $\approx 9^\circ$. The directional spreading width at the energy-weighted mean frequency—i.e., $\sigma_\theta(f_E)$ —determined via E-PSS is within 10° of the ADCP-derived estimate on average; furthermore, both estimates tend to follow the same general narrowing trend

486 with wind speed ($\approx 1.5^\circ / (\text{m s}^{-1})$). Although the locations and
 487 periods of operation are entirely different, this range of wave
 488 directional spread is consistent with values typically observed
 489 at the USACE FRF 8-m array [25], with $\sigma_\theta(f)$ ranging from
 490 25° at 0.1-0.12 Hz to 45° at 0.25 Hz.

491 *B. Impact on existing literature*

492 The superior performance of the empirical DoLP correction
 493 (relative to no correction and a solely laboratory-based
 494 correction) is part blessing and part curse. On the one hand,
 495 it offers a way to ensure that existing datasets obtained with
 496 single surface-looking polarimeters may produce results which
 497 are robust to external environmental factors. However, it also
 498 indicates that previous applications of PSS—which did not
 499 take steps to account for variation in ambient illumination—
 500 may need to be reevaluated in light of the present results.
 501 Based on our review of existing literature on the topic (much
 502 of it contributed by the authors of this paper), we find a range
 503 of potential impacts. The studies most negatively impacted
 504 by a systematic underestimation of surface wave slope (and
 505 amplified case-to-case variability) are those with results based
 506 on the absolute spectral energy density or integrated slope
 507 variance at short gravity and gravity-capillary scales. These
 508 include field observations made with no laboratory calibration
 509 [26] and field observations made with a laboratory calibration
 510 [8], [9]. However, in each of these cases, only a subset of the
 511 results were tied to the absolute magnitude of the slope spectral
 512 energy density. Many key results were based on the analysis
 513 of relative wave response, be it to hydrodynamic modulation
 514 [27] or suppression by surfactant slicks [10]. Many of the
 515 applications of PSS have bypassed this issue entirely, using
 516 the spatiotemporal propagation of the waves simply as a means
 517 to obtain the near-surface current [28], [29], [30], [31]; these
 518 results are entirely unaffected by the considerations mentioned
 519 here.

520 *C. Going forward*

521 In section I, we stated that the most complete form of PSS
 522 would entail simultaneous measurement of the sky-leaving,
 523 upwelling, and surface-reflected polarization state. Crucially,
 524 this would require an in-water sensor for obtaining measure-
 525 ments of upwelling radiance. It may be feasible to obtain a
 526 functionally similar base of information from two cameras,
 527 both surface-looking: (1) one with a field of view (FOV) de-
 528 termined by the wave scales one desires to resolve and (2) one
 529 with a wide FOV, broad enough to capture angles of incidence
 530 ranging from near-nadir to past Brewster's angle ($\approx 53^\circ$ for an
 531 air-water interface). The in-frame angles of incidence θ_i would
 532 be determined from the camera-lens combination's intrinsic
 533 and extrinsic parameters (i.e., through simple geometry). The
 534 wide-FOV polarimeter would then measure the variation of
 535 DoLP with θ_i that is particular to a given measurement; this
 536 would inherently include all effects related to the intensity and
 537 polarization state of sky-leaving and upwelling radiance. This
 538 field-determined DoLP(θ_i) would then be used as a 'lookup
 539 table', allowing one to directly compute DoLP in the narrow-
 540 FOV scene without reliance on dedicated measurements or

541 modeling of sky-leaving/upwelling radiance [32], [33] or any
 542 assumptions of theory. A demonstration of the sort of mea-
 543 surement which would enable this computation is provided
 544 in Figure 16. These observations were made on two non-
 545 consecutive days in Fall 2025 from the end of the pier in
 546 Piermont, NY, USA (incidentally, the same location used for
 547 the field validation exercise of Zappa *et al.* [2008], [3]).

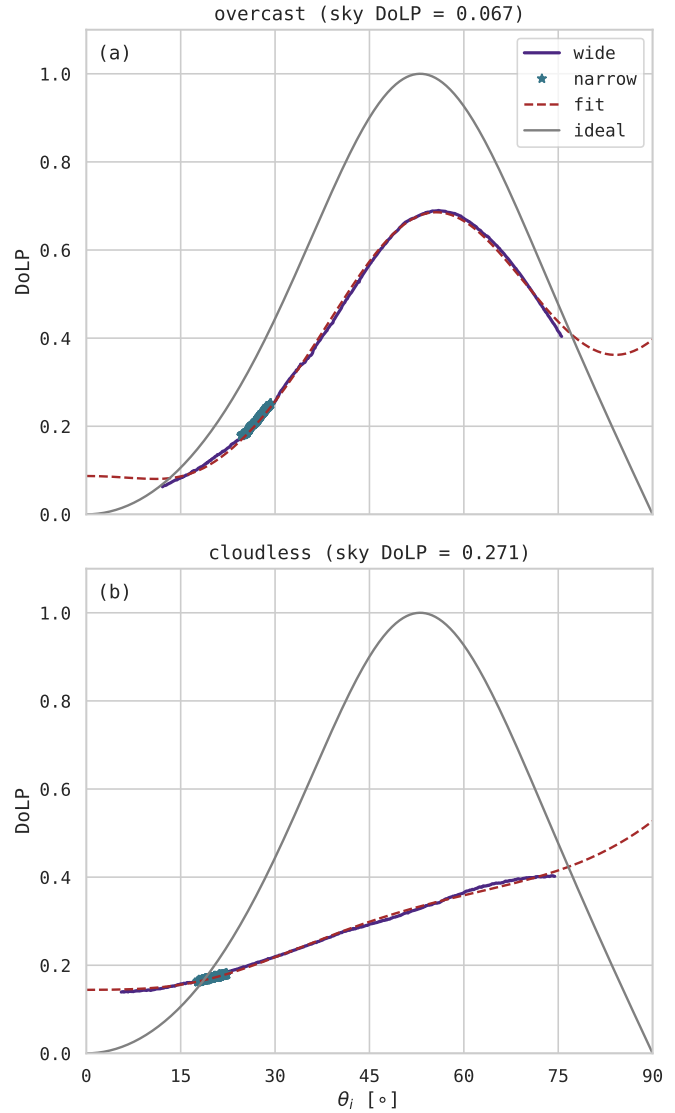


Fig. 16. Variation of DoLP with θ_i observed on days with (a) overcast and (b) cloudless sky conditions. On the overcast day, the least-squares fit determined $\hat{S}_{\text{sky}} = [1.000, 0.086, 0.017]$ (DoLP = 0.087) with an upwelling fraction of 0.058. On the cloudless day, the least-squares fit determined $\hat{S}_{\text{sky}} = [1.000, 0.117, 0.084]$ (DoLP = 0.144) with an upwelling fraction of 0.140.

548 For this demonstration, we made use of two azimuthally-
 549 aligned polarimetric cameras with identical Sony Polarsens
 550 DoFP polarimetric detectors. One camera was fitted with
 551 a narrow FOV lens (75 mm focal length, angles of view
 552 $6.5^\circ \times 5.4^\circ$) and the other was fitted with a wide FOV lens
 553 (5 mm focal length, angles of view $80.7^\circ \times 70.7^\circ$). We found
 554 the mean DoLP measurements made by the two cameras to be
 555 comparable within their overlapping look region. Furthermore,
 556 in applying a least-squares fit to the data assuming a framework

557 of specular reflection off the air-water interface, we were able
 558 to infer the Stokes vector of the sky-leaving radiance and
 559 the upwelling radiance fraction. It should be noted that the
 560 use of a wide-format lens may necessitate accounting for any
 561 effects resulting from light rays interacting obliquely with the
 562 polarizing filters on the focal plane array [34]. In any case,
 563 further testing of this two-camera concept is left to a future
 564 study.

565 V. SUMMARY

566 We have presented an extension of the polarimetric slope
 567 sensing (PSS) technique for measuring ocean surface waves.
 568 This technique has been named “extended polarimetric slope
 569 sensing”, or E-PSS; the “extended” modifier here denotes
 570 additional steps taken to

- 571 1) account for variation in ambient environmental conditions
- 572 2) allow one to infer the directional characteristics of surface
 573 gravity waves many times larger than the polarimeter field
 574 of view

575 When E-PSS is used with a simple empirical correction to
 576 the measured degree of linear polarization (DoLP), it is able
 577 to provide an accurate remote determination of the omnidi-
 578 rectional frequency spectrum across a wide range of surface
 579 wave frequencies (and therefore key sea state parameters,
 580 e.g. H_{m0}) from a single surface-looking imaging polarimeter.
 581 Further processing of the E-PSS outputs of water surface
 582 elevation and two-dimensional surface tilt yields a frequency-
 583 directional spectrum which is comparable to the spectrum
 584 obtained via a traditional ADCP-based approach. Crucially,
 585 these measurements are robust with respect to the ambient
 586 illumination condition. We find consistency in spectral energy
 587 density and equilibrium range slope between the long wave
 588 and short wave components of the omnidirectional frequency
 589 spectra produced by E-PSS. Furthermore, the short wave
 590 statistics obtained directly from the wave slope fields after
 591 empirical DoLP correction exhibit stronger agreement with
 592 classic observations than has been shown with the unadjusted
 593 results of previous applications of PSS. Finally, we present in
 594 concept an extension of this technique to involve two surface
 595 looking cameras, allowing for direct (in-scene) determination
 596 of the relationship between observed polarization state and
 597 surface inclination. This extension may improve performance
 598 in situations when the sky-leaving polarization state cannot be
 599 neglected, though that remains to be demonstrated at scale.

600 ACKNOWLEDGMENT

601 The ASIT2019 field observations were made with the as-
 602 sistance of Steve Faluotico, Jay Sisson, the crew of the *R/V*
 603 *Tioga*, and Carson Witte & Suki Wong. We thank Alejandro
 604 Cifuentes-Lorenzen for sharing the ADCP directional wave
 605 spectra used here. Collection of field data from ASIT was
 606 supported by NSF (Award Number 1756839), ONR (Award
 607 Number N00014-22-1-2183), and NASA (Award Number
 608 80NSSC19K1397). Analysis of the ASIT2019 dataset was
 609 supported by NSF award 20-49578 (NJML & CJZ). NJML
 610 was also supported by NSF award 23-40712.

611 The full suite of codes which contain our implemen-
 612 tation of Polarimetric Slope Sensing (PSS) for DoFP po-
 613 larimeters (as well as the additional modules which com-
 614 prise E-PSS) are available at <https://github.com/unh-cassll/polarimetric-slope-sensing>. All of the codes used to produce
 615 the graphics shown in this document are available within
 616 the following self-contained GitHub repository: https://github.com/unh-cassll/E-PSS_paper. These codes make use of data
 617 products stored at **DATA REPO (ZENODO)**.

618
 619

620

REFERENCES

- [1] A. Benetazzo, "Measurements of short water waves using stereo matched image sequences," *Coastal Engineering*, vol. 53, no. 12, pp. 1013–1032, Dec. 2006, publisher: Elsevier.
- [2] F. Bergamasco, A. Torsello, M. Sclavo, F. Barbariol, and A. Benetazzo, "WASS: An open-source pipeline for 3D stereo reconstruction of ocean waves," *Computers & Geosciences*, vol. 107, pp. 28–36, Oct. 2017.
- [3] C. J. Zappa, M. L. Banner, H. Schultz, A. Corrada-Emmanuel, L. B. Wolff, and J. Yalcin, "Retrieval of short ocean wave slope using polarimetric imaging," *Measurement Science and Technology*, vol. 19, no. 5, p. 055503, 2008, publisher: IOP Publishing ISBN: 0957-0233.
- [4] A. Benetazzo, F. Serafino, F. Bergamasco, G. Ludeno, F. Arduuin, P. Sutherland, M. Sclavo, and F. Barbariol, "Stereo imaging and X-band radar wave data fusion: An assessment," *Ocean Engineering*, vol. 152, pp. 346–352, Mar. 2018, publisher: Pergamon.
- [5] A. Lygre and H. E. Krogstad, "Maximum Entropy Estimation of the Directional Distribution in Ocean Wave Spectra," *Journal of Physical Oceanography*, vol. 16, no. 12, pp. 2052–2060, Dec. 1986, publisher: American Meteorological Society Section: Journal of Physical Oceanography.
- [6] D. H. Goldstein, *Polarized Light*, 3rd ed. Boca Raton: CRC Press, Jan. 2017.
- [7] K. J. Voss and Y. Liu, "Polarized radiance distribution measurements of skylight. I. System description and characterization," *Applied Optics*, vol. 36, no. 24, pp. 6083–6094, Aug. 1997, publisher: Optica Publishing Group.
- [8] C. J. Zappa, M. L. Banner, H. Schultz, J. R. Gemmrich, R. P. Morison, D. A. Lebel, and T. Dickey, "An overview of sea state conditions and air-sea fluxes during RaDyO," *Journal of Geophysical Research*, vol. 117, no. 5, 2012, publisher: Wiley Online Library.
- [9] N. J. M. Laxague, C. J. Zappa, D. A. LeBel, and M. L. Banner, "Spectral characteristics of gravity-capillary waves, with connections to wave growth and microbreaking," *Journal of Geophysical Research: Oceans*, vol. 123, no. 7, 2018, publisher: Wiley-Blackwell.
- [10] N. J. M. Laxague, C. J. Zappa, S. Soumya, and O. Wurl, "The suppression of ocean waves by biogenic slicks," *Journal of The Royal Society Interface*, vol. 21, no. 220, p. 20240385, Nov. 2024, publisher: Royal Society.
- [11] N. J. M. Laxague, Z. G. Duvarci, L. Hogan, S. P. Anderson, and C. J. Zappa, "The Effects of Subpixel Variability on Polarimetric Sensing of Ocean Waves," *IEEE Transactions on Geoscience and Remote Sensing*, vol. 63, pp. 1–13, 2025.
- [12] R. T. Guza and E. B. Thornton, "Local and shoaled comparisons of sea surface elevations, pressures, and velocities," *Journal of Geophysical Research: Oceans*, vol. 85, no. C3, pp. 1524–1530, 1980.
- [13] R. T. Frankot and R. Chellappa, "A Method for Enforcing Integrability in Shape from Shading Algorithms," *IEEE Transactions on Pattern Analysis and Machine Intelligence*, vol. 10, no. 4, pp. 439–451, 1988, ISBN: 0162-8828.
- [14] Y. You, G. W. Kattawar, K. J. Voss, P. Bhandari, J. Wei, M. Lewis, C. J. Zappa, and H. Schultz, "Polarized light field under dynamic ocean surfaces: Numerical modeling compared with measurements," *Journal of Geophysical Research*, vol. 116, no. C7, p. C00H05, Oct. 2011.
- [15] A. Ibrahim, A. Gilerson, T. Harmel, A. Tonizzo, J. Chowdhary, and S. Ahmed, "The relationship between upwelling underwater polarization and attenuation/absorption ratio," *Optics Express*, vol. 20, no. 23, pp. 25 662–25 680, Nov. 2012, publisher: Optica Publishing Group.
- [16] T. Elfouhaily, B. Chapron, K. B. Katsaros, and D. C. Vandemark, "A unified directional spectrum for long and short wind-driven waves," *Journal of Geophysical Research*, vol. 102, no. C7, pp. 15 781–15 796, 1997, publisher: Amer Geophysical Union.
- [17] C. Cox and W. Munk, "Measurement of the Roughness of the Sea Surface from Photographs of the Sun's Glitter," *Journal of the Optical Society of America*, vol. 44, no. 11, p. 838, 1954.
- [18] F. M. Bréon and N. Henriot, "Spaceborne observations of ocean glint reflectance and modeling of wave slope distributions," *Journal of Geophysical Research*, vol. 111, no. 6, 2006.
- [19] T. H. C. Herbers, R. L. Lowe, and R. T. Guza, "Field verification of acoustic Doppler surface gravity wave measurements," *Journal of Geophysical Research: Oceans*, vol. 96, no. C9, pp. 17 023–17 035, 1991.
- [20] Z. Lin, T. A. A. Adcock, and M. L. McAllister, "Estimating ocean wave directional spreading using wave following buoys: a comparison of experimental buoy and gauge data," *Journal of Ocean Engineering and Marine Energy*, vol. 8, no. 1, pp. 83–97, Feb. 2022.
- [21] M. D. Earle, "Nondirectional and Directional Wave Data Analysis Procedures," *National Data Buoy Center Technical Document*, vol. 03-01, p. 51, 2003. [Online]. Available: <https://www.ndbc.noaa.gov/wavemeas.pdf>
- [22] R. E. Jensen, V. Swail, and R. H. Bouchard, "Quantifying wave measurement differences in historical and present wave buoy systems," *Ocean Dynamics*, vol. 71, no. 6, pp. 731–755, Jul. 2021.
- [23] D. Peláez-Zapata, V. Pakrashi, and F. Dias, "Ocean Wave Directional Distribution from GPS Buoy Observations off the West Coast of Ireland: Assessment of a Wavelet-Based Method," *Journal of Atmospheric and Oceanic Technology*, vol. 41, no. 8, pp. 749–765, Aug. 2024, publisher: American Meteorological Society Section: Journal of Atmospheric and Oceanic Technology.
- [24] D. Peláez-Zapata and F. Dias, "EWDM: A wavelet-based method for estimating directional spectra of ocean waves," *Journal of Open Source Software*, vol. 10, no. 109, p. 7942, May 2025.
- [25] C. O. Collins, P. Dickhut, J. Thomson, T. de Paolo, M. Otero, S. Merrifield, E. Terrill, M. Schonau, L. Braasch, T. Paluszewicz, and L. Centurioni, "Performance of moored GPS wave buoys," *Coastal Engineering Journal*, vol. 66, no. 1, pp. 17–43, Jan. 2024.
- [26] N. J. M. Laxague, B. K. Haus, D. J. Bogucki, and T. M. Özgökmen, "Spectral characterization of fine-scale wind waves using shipboard optical polarimetry," *Journal of Geophysical Research*, vol. 120, no. 4, 2015.
- [27] N. J. M. Laxague, M. Curcic, J.-V. Björkqvist, and B. K. Haus, "Gravity-capillary wave spectral modulation by gravity waves," *IEEE Transactions on Geoscience and Remote Sensing*, vol. 55, no. 5, 2017, ISBN: 0196-2892 VO - PP.
- [28] N. J. M. Laxague, B. K. Haus, D. G. Ortiz-Suslow, C. J. Smith, G. Novelli, H. Dai, T. M. Özgökmen, and H. C. Gruber, "Passive optical sensing of the near-surface wind-driven current profile," *Journal of Atmospheric and Oceanic Technology*, vol. 34, no. 5, pp. 1097–1111, 2017.
- [29] N. J. M. Laxague, T. M. Özgökmen, B. K. Haus, G. Novelli, A. Y. Shcherbina, P. Sutherland, C. M. Guigand, B. Lund, S. Mehta, M. Alday, and J. Molemaker, "Observations of Near-Surface Current Shear Help Describe Oceanic Oil and Plastic Transport," *Geophysical Research Letters*, vol. 45, no. 1, 2018.
- [30] N. J. M. Laxague and C. J. Zappa, "Observations of mean and wave orbital flows in the ocean's upper centimetres," *Journal of Fluid Mechanics*, vol. 887, p. A10, Mar. 2020.
- [31] —, "The impact of rain on ocean surface waves and currents," *Geophysical Research Letters*, vol. 47, no. 7, p. e2020GL087287, Mar. 2020, publisher: John Wiley & Sons, Ltd.
- [32] R. Foster, A. Ibrahim, A. Gilerson, A. El-Habashi, C. Carrizo, and S. Ahmed, "Characterization of sun and sky glint from wind ruffled sea surfaces for improved estimation of polarized remote sensing reflectance," in *Polarization Science and Remote Sensing VII*, vol. 9613. SPIE, Sep. 2015, pp. 239–254.
- [33] R. Foster and A. Gilerson, "Polarized transfer functions of the ocean surface for above-surface determination of the vector submarine light field," *Applied Optics*, vol. 55, no. 33, pp. 9476–9494, Nov. 2016, publisher: Optica Publishing Group.
- [34] M. Pistellato and F. Bergamasco, "A Geometric Model for Polarization Imaging on Projective Cameras," *International Journal of Computer Vision*, May 2024.



Nathan J. M. Laxague (M '16) earned a Bachelor of Science in Physics in 2011 from the University of Miami, Coral Gables, FL USA. He received his Ph.D. in Applied Marine Physics from the Rosenstiel School of Marine and Atmospheric Sciences at the University of Miami in 2016. He was a postdoctoral research scientist at Lamont-Doherty Earth Observatory of Columbia University, in Palisades, NY, USA from 2017-2020. Since 2020, he has been an Assistant Professor of Ocean Engineering in the Department of Mechanical Engineering at the University of New Hampshire in Durham, NH, USA.

621

695

696

697

698

699

700

701

702

703

704

705

706

707

708

709

710

711

712

713

714

715

716

717

718

719

720

721

722

723

724

725

726

727

728

729

730

731

732

733

734

735

736

737

738

739

740

741

742

743

744

745

746

747

748

749

750

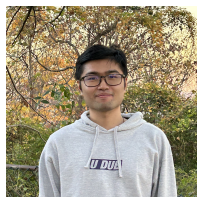
763
764
765
766
767
768

769

Z. Göksu Duvarci earned a Bachelor of Science in Chemical Engineering with a Minor in Mechanical Engineering in 2022 from Boğaziçi University in Istanbul, Turkey. She is currently a Ph.D. student in Ocean Engineering at the University of New Hampshire in Durham, NH, USA.

770
771
772
773
774
775
776
777
778
779
780

Lindsay Hogan (M '24) earned a Bachelor of Science in Geology and Geophysics in 2020 from Yale University, New Haven, CT, USA. She received a Masters by Research in Climate and Atmospheric Science in 2021 from the University of Leeds, Leeds, UK. Lindsay earned a Master of Arts in Earth and Environmental Sciences from Columbia University in New York, NY, USA in 2023 and is currently a Ph.D. Candidate in Earth and Environmental Sciences at Columbia University and Lamont-Doherty Earth Observatory in Palisades, NY, USA.

781
782
783
784
785
786
787
788
789
790

Junzhe Liu (M '25) earned a Bachelor of Science in Oceanography in 2022 from University of Washington, Seattle, WA, USA. He earned a Master of Arts in Earth and Environmental Sciences from Columbia University in New York, NY, USA in 2024 and is currently a Ph.D. Candidate in Earth and Environmental Sciences at Columbia University and Lamont-Doherty Earth Observatory in Palisades, NY, USA.

791
792
793
794
795
796
797
798
799
800
801
802

Christopher Bouillon earned a Bachelor of Engineering (B.Eng.) in Electrical Engineering in 2016 from Université de Sherbrooke. He received his Masters of Science in Physics from Université Laval, at the Centre for Optics, Photonics and Lasers (COPL). He obtained his Professional Engineering title (P. Eng.) from l'Ordre des Ingénieurs du Québec in 2025. He is currently a Ph.D. Candidate in Physical Oceanography at l'Institut des Sciences de la Mer (ISMER) of the Université du Québec à Rimouski, and a Lecturer in the Department of Mathematics,

Computer Science and Engineering.

803
804
805
806
807
808
809
810
811
812
813
814
815

Christopher J. Zappa (M '03) earned a Bachelor of Science in Mechanical Engineering in 1992 from Columbia University, NY, NY, USA. He received his Masters in Engineering in 1994 and his Ph.D. in Applied Ocean Physics in 1999 from the University of Washington, Seattle, WA, USA, and completed his Postdoctoral Scholar Award at the Woods Hole Oceanographic Institution in 2003 in Woods Hole, MA, USA. He is currently a Lamont Research Professor in and the Associate Director of Ocean and Climate Physics at Lamont-Doherty Earth Observatory in Palisades, NY, USA, and a Lecturer in the Department of Earth and Environmental Sciences in NY, NY, USA, both at Columbia University.